



Prandtl number dependence of flow topology in quasi-two-dimensional turbulent Rayleigh–Bénard convection

Ze-Hao Wang¹, Xin Chen^{2,1,†}, Ao Xu^{1,3} and Heng-Dong Xi^{1,3,†}

¹School of Aeronautics and Institute of Extreme Mechanics, Northwestern Polytechnical University, Xi'an 710072, PR China

²Shanghai Institute of Applied Mathematics and Mechanics and Shanghai Key Laboratory of Mechanics in Energy Engineering, School of Mechanics and Engineering Science, Shanghai University, Shanghai 200072, PR China

³National Key Laboratory of Aircraft Configuration Design, Northwestern Polytechnical University, Xi'an 710072, PR China

(Received 16 February 2024; revised 9 May 2024; accepted 1 June 2024)

To date, a comprehensive understanding of the influence of the Prandtl number (Pr) on flow topology in turbulent Rayleigh–Bénard convection (RBC) remains elusive. In this study, we present an experimental investigation into the evolution of flow topology in quasi-two-dimensional turbulent RBC with $7.0 \leq Pr \leq 244.2$ and $2.03 \times 10^8 \leq Ra \leq 2.81 \times 10^9$. Particle image velocimetry (PIV) measurements reveal the flow transitions from multiple-roll state to single-roll state with increasing Ra , and the transition is hindered with increasing Pr , i.e. the transitional Rayleigh number Ra_t increases with Pr . We mapped out a phase diagram on the flow topology change on Ra and Pr , and identified the scaling of Ra_t on Pr : $Ra_t \sim Pr^{0.93}$ in the low Pr range, and $Ra_t \sim Pr^{3.3}$ in the high Pr range. The scaling in the low Pr range is consistent with the model of balance of energy dissipation time and plume travel time that we proposed in our previous study, while the scaling in the high Pr range implies a new governing mechanism. For the first time, the scaling of Re on Ra and Pr is acquired through full-field PIV velocity measurement, $Re \sim Ra^{0.63} Pr^{-0.87}$. We also propose that increasing horizontal velocity promotes the formation of the large-scale circulation (LSC), especially for the high Pr case. Our proposal was verified by achieving LSC through introducing horizontal driving force Ra_H by tilting the convection cell with a small angle.

Key words: Bénard convection, turbulent convection

† Email addresses for correspondence: xinchen99@shu.edu.cn, hengdongxi@nwpu.edu.cn

1. Introduction

Thermally driven turbulence is a prevalent phenomenon observed in various natural systems, such as the ocean, atmosphere, and Earth's mantle. One extensively studied system for investigating thermally driven turbulence is turbulent Rayleigh–Bénard convection (RBC) (Ahlers, Grossmann & Lohse 2009; Lohse & Xia 2010; Chilla & Schumacher 2012; Xia 2013), where a fluid layer is heated from the bottom and cooled from the top, characterized by three control parameters: the Rayleigh number (Ra), the Prandtl number (Pr) and the aspect ratio (Γ). The Rayleigh number quantifies the strength of buoyancy force relative to thermal and viscous dissipative effects, and is given as $Ra = \alpha g \Delta T H^3 / (\nu \kappa)$. Here, α , ν and κ represent the thermal expansion coefficient, kinematic viscosity and thermal diffusivity of the fluid, respectively. The parameter g represents the gravitational acceleration, ΔT denotes the temperature contrast between the bottom and top plates, and H , L correspond to the height and length of the RBC system, respectively. The Prandtl number ($Pr = \nu / \kappa$) denotes the ratio of viscosity to thermal diffusivity, which characterizes the relative strength between momentum and thermal diffusion. The aspect ratio $\Gamma = L / H$ reflects the geometric constraints imposed by the boundary conditions of the system.

A fascinating feature of turbulent RBC is the emergence of a well-defined large-scale circulation (LSC) in the background of turbulent fluctuations. The LSC was initially observed by Krishnamurti & Howard (1981) through flow visualization. Subsequently, Cioni, Ciliberto & Sommeria (1996, 1997) directly measured the LSC using the multi-thermistor method. Their observations revealed that the LSC has complex dynamics including rotations and reversals. Qiu & Tong (2001) employed laser Doppler velocimetry in a cylindrical RBC cell to measure the velocity profile of the LSC. The results confirmed that the LSC maintains a large-scale quasi-two-dimensional (quasi-2-D) structure. Concerning the formation of LSC, Xi, Lam & Xia (2004) experimentally identified the dynamic process from the onset to the well-organized LSC in RBC. Utilizing shadowgraphs and particle image velocimetry (PIV), they revealed that thermal plumes initiate horizontal large-scale flow across the top and bottom plates. Over the past decades, LSC has attracted significant attention due to its intriguing dynamic features, including azimuthal rotation of the LSC plane (Brown & Ahlers 2006; Xi, Zhou & Xia 2006), coherent oscillation (Brown & Ahlers 2009; Xi *et al.* 2009; Chen *et al.* 2023), random and spontaneous cessations (momentary vanishing of its circulation speed; Brown & Ahlers 2006; Xi & Xia 2007; Xi *et al.* 2016), reversals (changes in its circulation directions) of LSC (Sugiyama *et al.* 2010; Chandra & Verma 2013; Chen *et al.* 2019), counter-flow orbiting of the vortex centre (Li *et al.* 2022), and the jump-rope motion of LSC (Vogt *et al.* 2018).

The formation of the LSC in a closed convection cell is commonly believed to be influenced by the geometry of the convection cell, as well as the values of Ra and Pr . In the case of a cell with $\Gamma = 1$, the expectation is that a single-roll LSC extends across the entire convection cell. As Γ increases ($\Gamma \geq 1$) or decreases ($\Gamma \leq 1$), it is intuitively anticipated that two or more circulation rolls may be present, either adjacent or superimposed upon each other. To investigate the impact of Γ on the LSC, van der Poel *et al.* (2012) numerically studied the flow state across the range $0.23 \leq \Gamma \leq 13$. Their study provided insights into the potential number of rolls that can exist at each Γ value. Recently, Wang *et al.* (2020) extended numerical investigations to a wider range of Γ values from 2 to 32. Their findings revealed the coexistence of multiple stable states with different roll size, and they presented a phase diagram that relates the size of the roll to Ra and Pr . Through theoretical analysis, they further explained that the elliptical

shape of the roll and viscous damping determine the size of the roll. In addition to the length-to-height ratio Γ , Huang *et al.* (2013) and Chong *et al.* (2018) observed that in a quasi-2-D convection cell, modifying the length-to-depth ratio can also alter the LSC, leading to a significant enhancement in heat transport.

Regarding the Ra dependence of the LSC, Xia, Sun & Zhou (2003) conducted PIV measurements in a quasi-2-D cell with Ra varying from 9×10^8 to 9×10^{11} . Their observations revealed that the LSC becomes increasingly concentrated near the perimeter of the cell as Ra increases, and the LSC persists for the highest value of Ra in their experiments. The 2-D numerical simulation by Zhu *et al.* (2018) addressed the question of the LSC's existence at even higher Ra . At $Ra = 1 \times 10^{14}$, they confirmed the continued presence of the LSC, albeit with much weaker and smaller structures. Expanding the exploration to lower Ra values, Chen *et al.* (2019) utilized PIV in a quasi-2-D cell to measure the LSC across an Ra range from 6.36×10^7 to 7.94×10^8 . They identified a gradual flow topology transition of the LSC from a four-roll state (FRS) to an abnormal single-roll state (ASRS), and eventually to the single-roll state (SRS) with increasing Ra . In addition to above-mentioned 2-D or quasi-2-D configurations, the cylindrical cell is another frequently explored geometry in studies of RBC. Wei (2021) measured the strength of a single roll against Ra over the wide range 1×10^3 to 1×10^9 using the multi-thermistor method. From the strength variations, seven distinct flow regimes were identified. Weiss & Ahlers (2011) investigated the LSC within a more slender cylindrical cell. Their findings confirmed the existence of a double-roll state (DRS) of the LSC, initially observed by Xi & Xia (2008). The proportion of time during which the DRS exists decreased from approximately 0.4 to approximately 0.06 as Ra increased from 2×10^8 to 1×10^{11} .

In contrast to the extensive studies regarding the Ra dependence of the LSC topology, understanding the effect of Pr on LSC topology appears limited. Existing studies are often confined to single Pr value, and frequently rely on indirect methods such as shadowgraph. For large Pr , Zhang, Childress & Libchaber (1997) identified the presence of LSC in a cubic cell under conditions of $Ra = 2.3 \times 10^8$ and $Pr = 895$ using shadowgraph. Similarly, Xi *et al.* (2004) conducted experiments in a cylindrical cell with $Ra = 6.8 \times 10^8$ and $Pr = 596$ through PIV, revealing the existence of a well-defined LSC. In contrast, Jiang, Sun & Calzavarini (2019) found no well-defined LSC in a quasi-2-D convection cell when $Ra = 5.0 \times 10^8$ and $Pr = 480$ by using shadowgraph. This observation was also supported by Li *et al.* (2021), who employed both shadowgraph and temperature measurements across an Ra range 6.0×10^8 to 3.0×10^{10} , and $11.7 \leq Pr \leq 650.7$. They revealed that as Pr increases, the LSC breaks down, leading to a regime transition in the Reynolds number (Re). In scenarios where Pr becomes extremely small, particularly when $Pr \ll 1$ – e.g. gallium or gallium-indium-tin (GaInSn) alloy with $Pr \sim 0.029$ – the opaqueness of the fluid poses a challenge. This hinders the direct velocity measurement of the entire flow field, making a comprehensive understanding of the impact of very small Pr on LSC elusive (Ren *et al.* 2022). Therefore, there is an urgent need for a comprehensive investigation of flow topology spanning a wide range of Pr , especially through the implementation of direct velocity measurements, such as PIV.

In this study, we systematically explore the evolution of the LSC topology in a quasi-2-D turbulent RBC. This investigation covers a broad range of Pr , varying from 7.0 to 244.2. Our primary objective is to provide the first direct full-field velocity measurement that illustrates how Pr influences the characteristics of the LSC. The rest of the paper is organized as follows. In § 2, we describe the experiment setup. In § 3, we present the experimental results and discussion. Finally, the conclusion of the study is drawn in § 4.

$H \times L \times W$	Pr	Ra	V_{gl}/V_f	$\rho (\times 10^3)$	$\alpha (\times 10^{-4})$	$\kappa (\times 10^{-7})$	$\nu (\times 10^{-6})$
20.0 × 20.0 × 6.0	7.0	2.29×10^8 – 2.81×10^9	0	0.998	2.07	1.43	1.00
12.6 × 12.6 × 3.8	13.5	3.05×10^8 – 6.10×10^8	0.20	1.057	3.41	1.28	1.73
20.0 × 20.0 × 6.0	34.6	6.03×10^8 – 1.02×10^9	0.42	1.117	4.82	1.14	4.00
20.0 × 20.0 × 6.0	61.7	2.88×10^8 – 1.15×10^9	0.52	1.145	5.32	1.08	6.68
25.5 × 25.5 × 7.7	94.3	5.50×10^8 – 1.82×10^9	0.62	1.167	5.69	1.04	9.78
25.5 × 25.5 × 7.7	128.5	4.01×10^8 – 1.43×10^9	0.62	1.171	5.69	1.03	13.3
25.5 × 25.5 × 7.7	148.3	2.94×10^8 – 1.76×10^9	0.62	1.174	5.69	1.03	15.3
25.5 × 25.5 × 7.7	244.2	2.03×10^8 – 1.60×10^9	0.71	1.193	5.95	1.00	24.3

Table 1. Geometrical information of the convection cells and parameters of the experiments. Here, H (cm), L (cm) and W (cm) are the height, length and width of the convection cell, respectively. The fluid properties of the mixture of glycerol and deionized water used in the present study are provided, where V_{gl}/V_f , ρ (kg m^{-3}), α (K^{-1}), κ ($\text{m}^2 \text{s}^{-1}$) and ν ($\text{m}^2 \text{s}^{-1}$) are the volume fraction of glycerol, and the density, thermal expansion coefficient, thermal diffusivity and kinematic viscosity of the water–glycerol mixture, respectively.

2. Experimental set-up and methods

In our experiments, three quasi-2-D rectangular convection cells of different sizes were employed. These cells are characterized by Plexiglas sidewalls and copper plates on the top and bottom. The heights (H) of the three cells are 12.6, 20.0 and 25.5 cm, respectively, and the height and length (L) are equal. The widths (W) of the cells are 3.8, 6.0 and 7.7 cm, respectively. Consequently, the aspect ratios for the cells are $\Gamma = L/H = 1$ and $\Gamma_{lateral} = W/H \approx 0.3$. The temperature of the top plate was controlled using a refrigerated circulator (PolyScience), while two resistive film heaters maintained constant power input to heat the bottom plate. Temperature measurements were obtained by 12 thermistors, each with diameter 2.5 mm, embedded in the plates. These thermistors are positioned approximately 8 mm away from the fluid–solid interface. Three pairs of thermistors embedded in the bottom plate are spaced along the L direction at $L/4$, $L/2$ and $3L/4$, with the same arrangement for three pairs of thermistors in the top plate. The working fluid employed was a mixture of glycerol and deionized water with varying ratio. The experiments covered an Ra range 2.03×10^8 – 2.81×10^9 and a Pr range 7.0–244.2 (refer to table 1 for detailed geometrical information about the convection cells and the corresponding parameters).

The PIV technique was employed to measure the flow field in the vertical mid-plane of the RBC cell. To minimize the influence of surrounding temperature fluctuations and heat leakage, all PIV measurements were conducted within a custom-made thermostat box. The PIV system is composed of several key components: a dual Nd:YAG laser (Beamtech Vlite-200) with power output 200 mJ per pulse, a CCD camera (Flowsense EO 4M) with a 16-bit dynamic range and spatial resolution 2048×2048 pixels, a synchronizer, and control software that includes a PIV analysis platform (Dantec DynamicStudio). A laser sheet with thickness approximately 1 mm illuminates the seeding particles in the vertical mid-plane of the RBC cell. Seeding particles, with diameter $5 \mu\text{m}$, are polyamid particles with density in the range 1.02–1.05 g cm^{-3} . The Stokes number (St) is used to characterize the behaviour of particles suspended in a fluid flow, which is defined as the ratio of the characteristic time t_0 of a particle to a characteristic time t_f of the flow. For $St \ll 1$, particles are considered to closely follow fluid streamlines (Tropea, Yarin & Foss 2007). In the RBC system, the Kolmogorov time scale ($\tau_\eta = (\nu/\epsilon)^{1/2}$) can be used as the

characteristic time of the flow. Here, the energy dissipation rate ϵ has an exact relation in RBC: $\epsilon = \nu \kappa^2 Ra (Nu - 1)/H^4$. The characteristic time of the seeding particle can be calculated by $t_0 = \rho_p d_p^2 / (18 \rho \nu)$, where ρ_p and d_p are the density and the diameter of the seeding particle. In our experiments, the maximum calculated Stokes number is 2.16×10^{-6} for $Ra = 2.81 \times 10^9$, $Pr = 7.0$, which is indeed very small. Therefore, in the current studies, the seeding particles can closely follow the fluid. Each PIV measurement session lasts for at least 2 hours, and a minimum of 7200 snapshots were acquired at sampling rate 1 Hz.

3. Results

3.1. The Pr dependence of the flow topology evolution

We first compare the flow topology at different values of Pr . Figure 1 presents the velocity field obtained through PIV measurements, averaged over a short time period, at $Pr = 7.0$, 128.5 and 244.2, respectively, within the similar range of Ra . The short-time averaged velocity fields presented here are essentially instantaneous snapshots. The purpose of applying a short-time average to the instantaneous snapshots is to enhance the clarity of the flow field. However, it is important to note that even with this short-time averaging, the flow fields maintain their instantaneous nature, albeit with a clearer and more distinct flow topology. During averaging process, we ensured that there were no flow reversals within the short time period. As an instantaneous velocity map may not reflect the main feature of the flow, the selection of the short-time averaged velocity maps is based on the mean flow structure, i.e. the dominant Fourier mode from the time average of all the flow modes of the entire PIV measurement at each Ra (usually lasts for 2–3 hours), which is presented in figure 2. If the single-roll formed LSC exists, then the short time period used for averaging corresponds to one turnover time of the LSC. In cases where there is no LSC but the flow exhibits multicellular structures, the short time period is determined by the typical circulation time of a cellular flow structure. In fact, the multicellular flow structure remains quite stable for an extended duration in our experiments, making the choice of the average time less critical. For $Pr = 7.0$, figures 1(a,d,g,j,m) illustrate a typical transition in flow topology from an abnormal single-roll state (ASRS) (figure 1a) to a single-roll state (SRS) (figures 1d,g,j,m), as previously observed by Chen *et al.* (2019). The ASRS is characterized by the presence of a large vortex in the flow field, with the interior of this vortex splitting into two smaller vortices. The formation of substructures within the large vortex arises from the balance between plume travel and plume dissipation time. The SRS, commonly observed in earlier studies (Xia *et al.* 2003; Sugiyama *et al.* 2010), consists of a main vortex with two small corner vortices in the tilted-ellipse shape.

As Pr is increased to 128.5, the flow topology exhibits distinct difference compared with the $Pr = 7.0$ case, as shown in figures 1(b,e,h,k,n). At $Ra = 2 \times 10^8$, the mean field displays a side-by-side four-roll state (sFRS) (figure 1b). This state is characterized by the presence of four slender rolls arranged horizontally adjacent to each other within the flow. For $Ra = 4.01 \times 10^8$, the flow is dominated by strong vertical motions and exhibits a double-roll state (DRS) (figure 1e), with downward flow at the centre of the cell, and upward flow near the sidewalls. It is worthwhile to note that during the measurement time, no reversal is observed for the sFRS and the DRS. Further increasing Ra to 7.42×10^8 , the mean field transitions to a distinct four-roll state (FRS), diverging from the aforementioned sFRS. Earlier studies suggested that the FRS could arise from the superposition of two LSC flow fields with opposite directions due to frequent flow reversals (Chong *et al.* 2018).

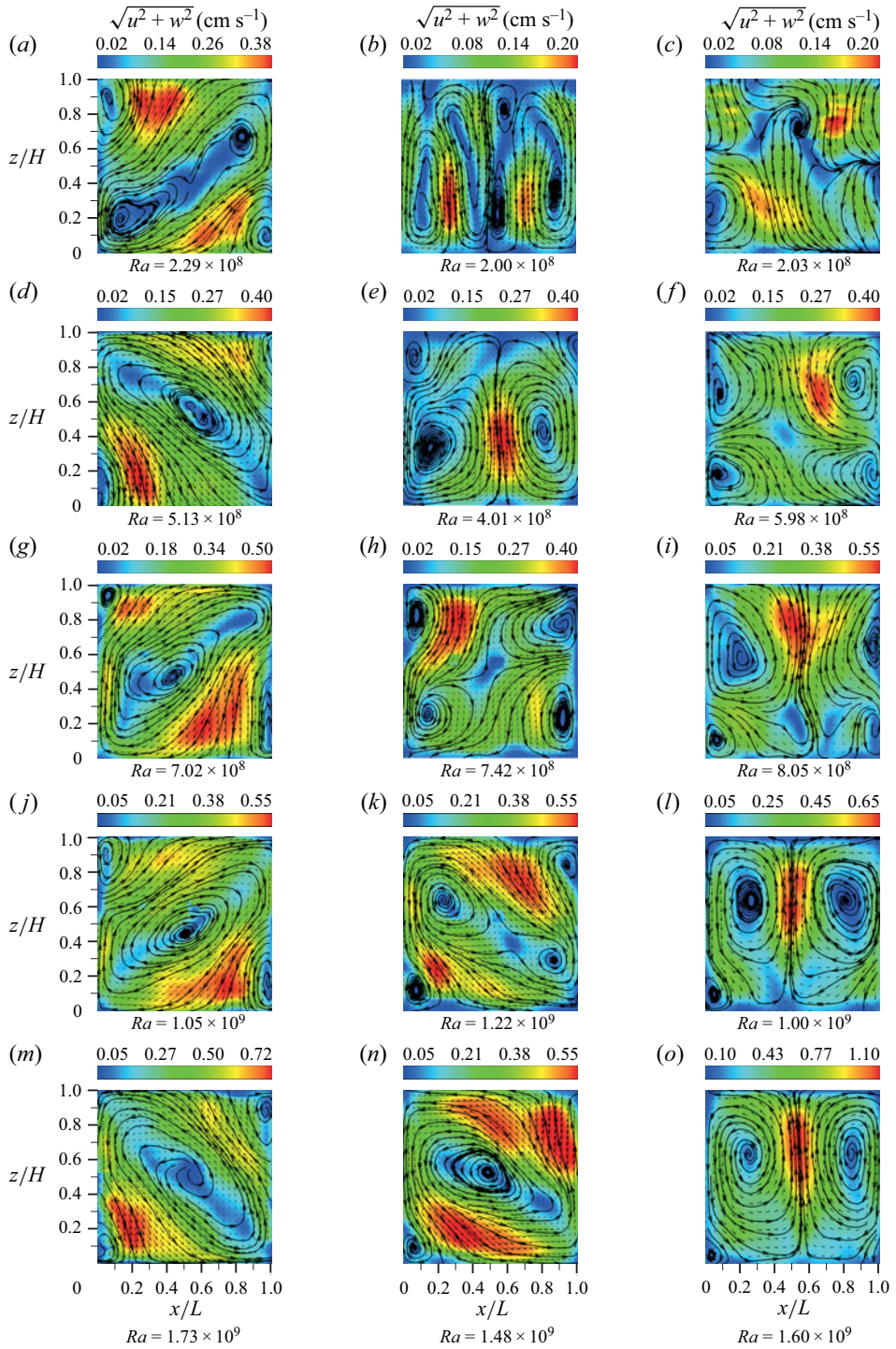


Figure 1. Short-time averaged PIV velocity maps with streamlines for different Ra and Pr , where u and w are horizontal and vertical components of the velocity: (a,d,g,j,m) $Pr = 7.0$, (b,e,h,k,n) $Pr = 128.5$, (c,f,i,l,o) $Pr = 244.2$.

Pr dependence of flow topology in quasi-2-D RB convection

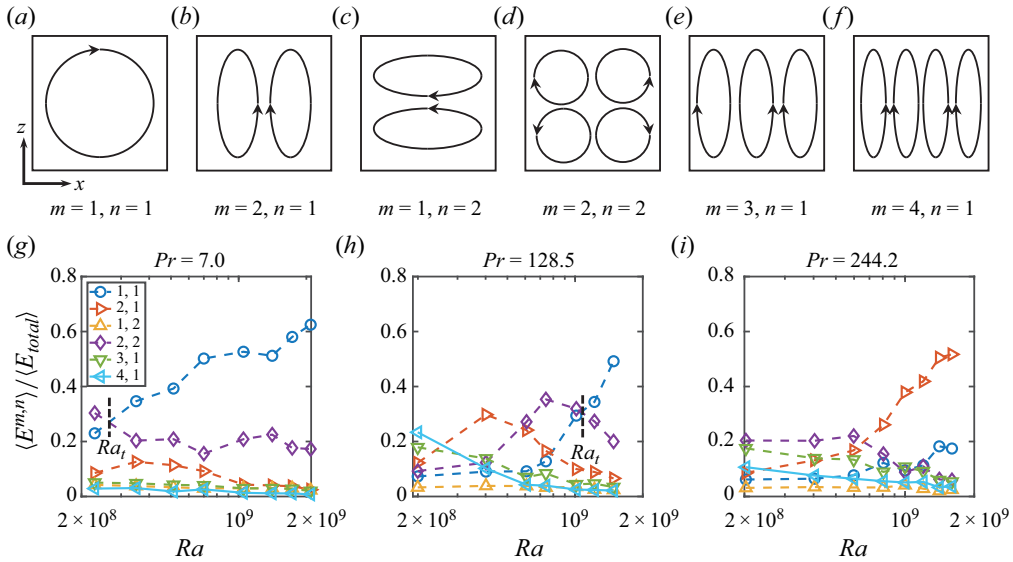


Figure 2. (a–f) Cartoon patterns of the six Fourier modes of the velocity fields. (g–i) Time-averaged energy contained in each flow mode as a function of Ra for $Pr = 7.0, 128.5, 244.2$, respectively. The dashed line represents the value of Ra where the crossover between (2, 2) mode and (1, 1) mode occurs (i.e. Ra_t).

However, in this study, all flow fields are averaged within a short time interval, during which no flow reversal occurs. The FRS is quite stable; even when averaging the flow field over the entire measurement period, it remains in the FRS. As Ra is increased further, the flow topology transitions from FRS to ASRS and eventually to SRS, similar to the case $Pr = 7.0$. To the best of our knowledge, this is the first observation of sFRS and DRS in a convection cell with $\Gamma = 1$. Another important finding is that the transitional Ra corresponding to the transition from ASRS to SRS differs between $Pr = 7.0$ and $Pr = 128.5$. For $Pr = 7.0$, the transition occurs between $Ra = 2.29 \times 10^8$ (figure 1a) and $Ra = 5.13 \times 10^8$ (figure 1d), while for $Pr = 128.5$, it occurs between $Ra = 1.22 \times 10^9$ (figure 1k) and $Ra = 1.48 \times 10^9$ (figure 1n). This suggests that a higher Ra is required to establish a well-defined LSC at higher Pr .

As Pr increases to 244.2, the evolution of flow topology follows a different route compared to the cases $Pr = 7$ and $Pr = 128.5$. With increasing Ra , the flow field gradually transitions from FRS to DRS. In the FRS, the two upper rolls progressively grow in size and compress the two lower rolls until $Ra = 1.0 \times 10^9$, where the two upper rolls occupy nearly the entire cell. The DRS persists throughout our experiments, even at the highest Ra values. Interestingly, the DRS observed at $Pr = 244.2$ has the direction opposite to that observed at $Pr = 128.5$ (figure 1e). Furthermore, the direction of the DRS remains consistent throughout current measurement, which lasts for almost 2 days. A similar DRS flow field was reported by Li *et al.* (2021) at $Ra = 1.4 \times 10^{10}$ and $Pr = 345.2$ using shadowgraph visualization. They observed clusters of plumes rising from the middle of the lower plate in the convection cell. However, we currently lack an understanding of the differences between these two types of DRS (figures 1e,o) and whether a flow reversal also exists in the DRS. This aspect certainly demands further investigation in future studies.

To qualitatively analyse the flow topology, we examine the flow energy using Fourier mode decomposition (Chandra & Verma 2011; Wagner & Shishkina 2013;

Chong *et al.* 2018). In this approach, each instantaneous velocity field (u_x, u_z) is projected onto the Fourier modes as follows:

$$u_x^{m,n} = 2 \sin(m\pi x) \cos(n\pi z), \quad (3.1)$$

$$u_z^{m,n} = -2 \cos(m\pi x) \sin(n\pi z). \quad (3.2)$$

Typically the first four modes are considered (i.e. $m, n = 1, 2$). In this study, considering the observed sFRS, we also include the modes with $m = 3, 4$ and $n = 1$. The instantaneous amplitude of each mode $A^{m,n}(t)$ is obtained by projecting the velocity field components onto the corresponding Fourier modes: $A^{m,n}(t) = \langle u_x(t) u_x^{m,n} \rangle_{x,z} + \langle u_z(t) u_z^{m,n} \rangle_{x,z}$. Consequently, the energy of each flow mode can be evaluated as $E^{m,n}(t) = [A^{m,n}(t)]^2$ (Xi *et al.* 2016).

Figures 2(g–i) show the mean energy contained in each of the six Fourier modes as a function of Ra . Here, the mean energy contained within each of the six Fourier modes is computed by averaging over the entire measurement period. For $Pr = 7.0$, the (1, 1) and (2, 2) modes contain the majority of the energy, while the (1, 2), (3, 1) and (4, 1) modes remain negligibly weak throughout the entire range of Ra . As Ra increases, the energy of the (2, 2) mode decreases, while the energy of the (1, 1) mode increases. There exists a crossover Ra value (Ra_t) between the (2, 2) mode and the (1, 1) mode. When Ra is below Ra_t , the (2, 2) mode dominates the flow field, but the (1, 1) mode remains comparable. In this situation, the flow field corresponds to the ASRS. When Ra is larger than Ra_t , the (1, 1) mode surpasses the (2, 2) mode and becomes dominant, resulting in the flow transition to the SRS.

As Pr increases to 128.5 (figure 2h), the evolution of each mode with Ra becomes more complex. For the lowest Ra , the (4, 1) mode has the highest energy among all modes, consistent with the sFRS flow field shown in figure 1(b). As Ra further increases, the (4, 1) mode is surpassed by the (2, 1) mode, which dominates the flow field until the (2, 2) mode overtakes the (2, 1) mode. Before this transition, the flow field corresponds to the DRS. Once the (2, 2) mode begins to dominate the flow field, the energy of the (1, 1) mode starts to increase rapidly with increasing Ra . When Ra exceeds Ra_t , the (1, 1) mode becomes dominant, and the flow field eventually evolves from ASRS into the SRS. The evolution of the mode energy with Ra shown in figure 2(h) is consistent with the flow field evolution illustrated in figure 1.

At $Pr = 244.2$ (figure 2i), the flow field undergoes a transition from dominance of the (2, 2) mode to dominance of the (2, 1) mode, which is consistent with the FRS to DRS transition observed in figure 1. Additionally, we observe that there exists a critical Ra (approximately $Ra = 6 \times 10^8$) for the (1, 1) and (2, 2) modes. The values of the (1, 1) and (2, 2) modes remain almost unchanged when $Ra \leq 6 \times 10^8$. In contrast to the (1, 1) and (2, 2) modes, the value of the (2, 1) mode increases with increasing Ra , while the values of the (3, 1) and (4, 1) modes decrease. Although there are distinct differences in the evolution of each mode at different Pr , there is a one-to-one correspondence between the flow mode and the flow topology.

One may observe that in the cases with relative low Ra at higher Pr , such as those shown in figures 1(b,c), the velocity fields are relatively chaotic, distinguishing them from cases with higher Ra . This distinction can be attributed to the results presented in figures 2(h,i), where for small Ra , several flow modes are comparable to each other in terms of the energy contained in each mode, thus the flow structure is a composition of the different flow modes, resulting in a relatively chaotic flow field. However, as Ra increases, certain flow modes (e.g. (1, 1) or (2, 1)) start to dominate the flow field more prominently than

other modes, leading to a clearer and more distinct flow field. Concerning the flow fields shown in figures 1(b,c), we chose to make the average of the instantaneous snapshots over a short time period where the (4, 1) and (2, 2) modes dominate in the flow field compared to other flow modes, respectively. This method of selection ensures that the obtained flow field is a representative of the averaged (over the entire measurement) energy contained in each Fourier modes, i.e. a typical flow field at the specific control parameters.

We employ the dominance of the (1, 1) mode as the criterion for determining the existence of a well-defined LSC in the system, with the corresponding Ra value denoted as the transitional Ra (Ra_t). This transition is marked by the black dashed line in figures 2(g,h). Comparing figures 2(g) and 2(h), we observe that $Ra_t = 2.71 \times 10^8$ for $Pr = 7.0$, significantly smaller than $Ra_t = 1.12 \times 10^9$ for $Pr = 128.5$. This observation is in line with the fact that the transition from ASRS to SRS in figure 1 occurs at smaller Ra for $Pr = 7.0$ compared to that for $Pr = 128.5$. In other words, a higher Ra is required to form LSC for higher Pr . This may explain why we do not observe an LSC at $Pr = 244.2$, as the driving force (Ra) of the system may not be sufficient within the current range of Ra . We propose that the DRS is only a transitional state, and the LSC would likely emerge with further increase in Ra at $Pr = 244.2$. However, the size of the current experimental set-up imposes limitations on further increasing Ra .

To further explore the influence of Pr on the flow field, and examine the trend of Ra_t on Pr , we extended the range of Pr and constructed a phase diagram of dominant Fourier modes across a broad $Ra-Pr$ parameter space, as shown in figure 3. The phase diagram reveals that at low Pr , the system predominantly exhibits two modes: (2, 2) and (1, 1). As Pr increases, new dominant modes emerge, namely (4, 1) and (2, 1), as shown in figures 1(b,e,l,o). The Ra_t value, corresponding to the transition from the dominance of the (2, 2) mode to the (1, 1) mode, tends to increase with Pr . The increase of Ra_t with increasing Pr has two distinct regimes: a slow increase when $Pr \leq 13.5$, characterized by scaling slope 0.93, and a fast increase when $Pr \geq 13.5$, exhibiting a steeper scaling slope 3.3. To examine the scaling relationship between Ra_t and Pr , Chen *et al.* (2019) proposed a time scale balance model in which the transition of the flow occurs when the plume kinetic energy dissipation (by viscosity) time is comparable to the time scale for the plume ascending or descending to the mid-height of the cell. This led to a scaling relationship $Ra_t \sim Pr^{1.06}$, closely matching their experimentally observed relationship $Ra_t \sim Pr^{1.12 \pm 0.07}$ within a narrow Pr range $4.3 \leq Pr \leq 7.0$. In our current study, we validate the persistence of this scaling relationship between Ra_t and Pr in a wider Pr range $Pr \leq 13.5$, with the scaling exponent being $1/0.93 = 1.08$, as shown by the black solid line in figure 3.

As Pr exceeds 13.5, the Pr dependence of Ra_t becomes less prominent compared to the moderate Pr range. For instance, at $Pr = 13.5$, Ra_t is 5.67×10^8 , while at $Pr = 148.3$, a tenfold increase, Ra_t is increased only approximately twofold, i.e. 1.19×10^9 , indicating a relatively small change in Ra_t despite the substantial change in Pr . To explore this behaviour, we examine the Grashof number ($Gr = \alpha g \Delta T H^3 / \nu^2 = Ra/Pr$), which represents the ratio of buoyancy to viscous forces (the corresponding $Gr-Pr$ phase diagram is provided in figure 8 in the Appendix). In our quasi-2-D study, the viscous force encompasses both internal fluid viscosity and the sidewall-induced viscous force. The previously deduced relationship $Ra_t \sim Pr^{1.06}$ at moderate Pr can be expressed in terms of Gr as $Gr_t \sim Pr^{0.06}$. The weak Pr dependence of Gr_t at moderate Pr implies that the transitional Gr_t remains relatively constant with varying Pr , indicating the existence of a critical Gr threshold governing the transition from the dominance of the (2, 2) mode to

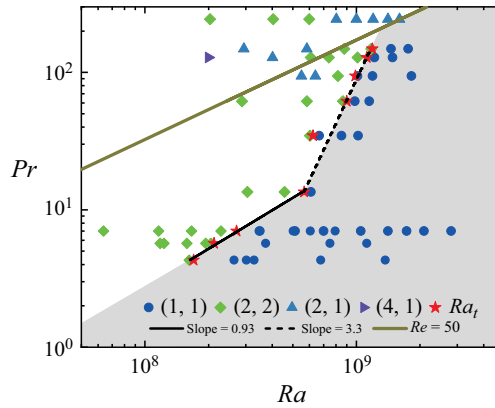


Figure 3. Phase diagram of the dominant Fourier modes in the $Ra-Pr$ parameter space. The stars indicate the transitional Ra_t . The black solid line and dashed line have slopes 0.93 and 3.3, respectively. The brown solid line is $Re = 50$, where $Re = 9.4 \times 10^{-3} Ra^{0.63} Pr^{-0.87}$ (see § 3.2 for description). The area above the brown solid line is where $Re \leq 50$. The shaded region represents the dominance of the (1, 1) mode. The data for $Pr = 4.3, 5.7$ and 7.0 from Chen *et al.* (2019) are also included.

the (1, 1) mode. Beyond this threshold, characterized by the nearly invariant Gr_t , the flow structure transforms into a single-roll form of the LSC or a (1, 1)-mode-dominated flow field. The measured $Pr \sim Ra_i^{3.3}$ in the large Pr range can also be expressed in terms of Gr_t scaling as $Gr_t \sim Pr^{-0.7}$. In contrast to the small but positive exponent in the moderate Pr range, the negative exponent at high Pr indicates that with increasing Pr , the transitional Gr_t decreases. From table 1, we can observe that the increase of Pr is accompanied by an increase in viscosity, while thermal diffusivity remains relatively constant. In this high- Pr regime ($Pr \geq 13.5$), Gr is no longer approximately constant – i.e. the speed with which the buoyancy increases is slower than that of the viscous force – which suggests a different mechanism governing the formation of the (1, 1)-dominated flow state. Indeed, the distinct mechanism observed in the high- Pr regime merits deeper investigation in future studies.

3.2. The Ra and Pr dependence of the Reynolds number

As PIV provides direct measurement of the flow field, we can now investigate the Ra and Pr dependence of Re more directly than in methods relying on local velocity measurements (Lam *et al.* 2002) or cross-correlation between adjacent thermistors (Li *et al.* 2021). In our study, we define the Reynolds number (Re) as $Re = \sqrt{\langle u^2 + w^2 \rangle_{V,t}} H/\nu$, where $\langle \rangle_{V,t}$ represents the spatial average over the measuring plane and time average. Figure 4(a) shows the Ra dependence of Re at different Pr based on the PIV velocity maps. First, we can observe a monotonic decrease in Re with increasing Pr , which is consistent with previous studies (Chen, Wang & Xi 2020; Li *et al.* 2021). Second, slight variations in the power-law exponent (γ) are noted in the $Re \sim Ra^\gamma$ scaling law for different Pr values, falling within the range $0.50 \leq \gamma \leq 0.74$. This range aligns with the values $0.53 \leq \gamma \leq 0.74$ reported by Li *et al.* (2021) for $11.7 \leq Pr \leq 650.7$, and $0.50 \leq \gamma \leq 0.68$ reported by Lam *et al.* (2002) for $6 \leq Pr \leq 1027$. Specific differences in γ for each Pr are attributed to different calculation methods used for Re . For example, Li *et al.* (2021) employed the plume velocity obtained from cross-correlation of temperature probes as the characteristic

Pr dependence of flow topology in quasi-2-D RB convection

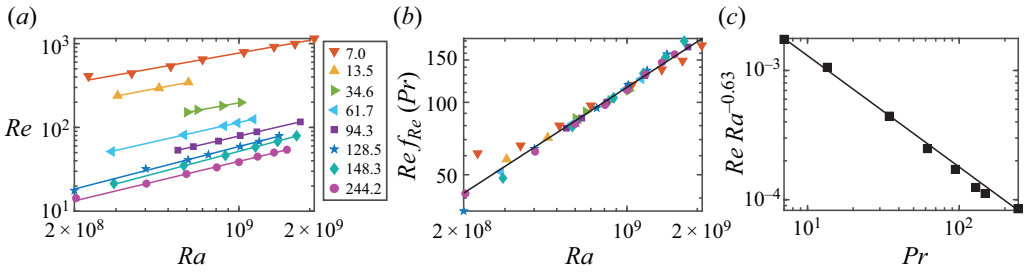


Figure 4. (a) Plots of Re as a function of Ra for different Pr . (b) Plots of $Re f_{Re}(Pr)$ as a function of Ra , where $f_{Re}(Pr)$ is a coefficient used to make all the Re data collapse to a master line. Note that the coefficient $f_{Re}(Pr)$ depends only on Pr , and is therefore a constant for each Pr . The solid line is the power-law fit to the data, yielding $Re f_{Re}(Pr) = 2.5 \times 10^{-4} Ra^{0.63 \pm 0.03}$. (c) Plot of $Re Ra^{-0.63}$ as a function of Pr . The data are mean values of $Re Ra^{-0.63}$ averaged over all the Ra for each Pr . The solid line is the power-law fit to the data, yielding $Re Ra^{-0.63} = 9.4 \times 10^{-3} Pr^{-0.87 \pm 0.06}$.

velocity, while Lam *et al.* (2002) utilized the maximum velocity measured by laser Doppler velocimetry as the characteristic velocity. Additionally, all three studies, including ours, Li *et al.* (2021) and Lam *et al.* (2002), share the same increasing trend of γ with increasing Pr .

To establish a relationship for $Re \sim Ra^\gamma Pr^\beta$ within the range $7.0 \leq Pr \leq 244.2$, we adopt the method proposed by Xia, Lam & Zhou (2002). We introduce a factor $f_{Re}(Pr)$ that multiplies Re , resulting in values of $f_{Re}(Pr)$ at different Pr collapsing onto a single line (see figure 4b). Note that the coefficient $f_{Re}(Pr)$ depends only on Pr and remains unchanged across different Ra values. Once $f_{Re}(Pr)$ is determined, we fit a straight line to all data points in figure 4(b), yielding $Re f_{Re}(Pr) \sim Ra^{0.63 \pm 0.03}$. Next, we normalize Re by $Ra^{-0.63}$ and average the data for each Pr , as shown in figure 4(c). From this analysis, we obtain $Re Ra^{-0.63} \sim Pr^{-0.87 \pm 0.06}$. Thus for the current experiments, we directly measured $Re \sim Ra^{0.63 \pm 0.03} Pr^{-0.87 \pm 0.06}$. Comparing our results to recent experimental Re measurements by Li *et al.* (2021), covering the Pr range 11.7 to 145.7, and revealing that $Re \sim Ra^{0.58 \pm 0.01} Pr^{-0.82 \pm 0.04}$, we observe good agreement between the two measurements. For the first time, the Ra and Pr dependence of Re through direct velocity measurements of the full flow field is obtained (see table 2 in the Appendix for detailed values).

Li *et al.* (2021) observed a significant drop in the magnitude of Re at $Pr = 345.2$ and 650.7, and this transition was attributed to the breakdown of the LSC. Since the Pr values at which Li *et al.* (2021) observed the dramatic drop in Re are beyond our Pr range, we cannot determine whether there are different mechanisms behind such transitions. It is important to note that while Li *et al.* (2021) used an indirect velocimetry method based on temperature signal correlation, their results exhibit almost the same scaling as our current study. However, the method of determining velocity through cross-correlation of temperature signals typically relies on a long-time sequence of data to accurately converge the cross-correlation function and thereafter determine the time delay between thermistors. Furthermore, in cases where the flow field exhibits multiple rolls, such as the (2, 2)-mode-like flow, two thermistors may locate in different rolls, leading to less predominant cross-correlation signals. This limitation can be mitigated by using very-long-time measurements. On the other hand, using a direct PIV method avoids these issues as velocity is measured directly, which in turn assures the accuracy

for determining Re . Therefore, we are well positioned to provide the non-ambiguous relationship between Re and Ra , and in addition review the key assumption in the well-adopted Grossmann–Lohse (GL) theory (Grossmann & Lohse 2000), namely the presence of LSC or the ‘wind of turbulence’. The GL model predicted the Ra and Pr dependence of Re based on this assumption. As shown in figures 3 and 4, it is evident that despite variations in the flow structure, whether the single-roll form of LSC exists or not, the GL model’s prediction on Re remains valid. It is important to note that current results do not imply that the assumption in the GL model is not necessary; on the contrary, we believe that this assumption of the existence of LSC can be expanded to include not only a single-roll form of LSC but also a multiple-roll form of LSC. In the original paper by Grossmann & Lohse (2000), the existence of LSC was associated with two key effects. First, it leads to the build-up of a shear boundary layer between the LSC and the boundary. Second, it induces stirring of the fluid in the bulk region. Considering these effects, it becomes clear that in the multiple-roll flow states presented in the current study, the shear boundary layer continues to develop, although the shear boundary layers may vary in direction when multiple rolls are adjacent to each other. Furthermore, the fluid in the bulk experiences stirring effects either from within an individual roll or through interactions between adjacent rolls. Consequently, the results presented in our study are consistent with the principles of the GL theory and represent a more general form, rather than negating the initial assumption regarding LSC.

3.3. The evolution of flow topology with cell tilting

From the flow field shown in figure 1, we can see that the DRS (figures 1*e,i,l,o*) and sFRS (figure 1*b*) are characterized by concentrated regions of very high vertical velocity, and the weight of the vertical velocity is much higher than that of the horizontal velocity in the flow. In contrast, the SRS (figures 1*d,g,j,m,n*) exhibits a more uniform distribution of regions with high velocity and low velocity, and the weight of the vertical velocity is comparable to that of the horizontal velocity in the flow. Given these observations, it is natural to assume that the relative weight of the vertical and horizontal velocities is directly related to the formation of a SRS or multiple-roll state (MRS). Specifically, one may wonder if we increase the weight of the horizontal velocity in the MRS, whether the flow field would transition to SRS.

To address this question, we conducted an experiment at $Pr = 244.2$ with a convection cell tilted by a small angle (1.5°), as illustrated in figure 5(*a*). When the convection cell is tilted, Ra can be decomposed into vertical (Ra_V) and horizontal (Ra_H) components (Zhang, Ding & Xia 2021). Specifically, $Ra_V = Ra \cos \beta$ and $Ra_H = Ra \sin \beta$, where V represents the vertical direction, H represents the horizontal direction, and β denotes the tilt angle of the convection cell with respect to the horizontal direction. To compare the flow field with the case at $\beta = 0$, we controlled Ra_V at $\beta = 1.5^\circ$ to be equal to the original Ra at $\beta = 0$. In other words, the driving force in the vertical direction of the convection cell was kept constant. The range of Ra_V that we explored is from 2.03×10^8 to 1.60×10^9 . As a result, $Ra_H = \tan 1.5^\circ Ra_V \approx 0.026 Ra_V$, leading to range $5.28 \times 10^6 \leq Ra_H \leq 4.16 \times 10^7$. After applying Ra_H in the horizontal direction of the convection cell, we observed a distinct change in the flow field at $Pr = 244.2$: the flow field transitions from MRS to SRS. This implies that our conjecture of increase in the horizontal velocity of the flow inducing the SRS is correct. The appearance of the SRS when the cell is tilted at high Pr also aligns with the prediction made by Grossmann & Lohse (2000). In their work, they proposed the idea of slightly tilting the cell to induce LSC when $Pr \gg 7$. This finding also agrees with

Pr dependence of flow topology in quasi-2-D RB convection

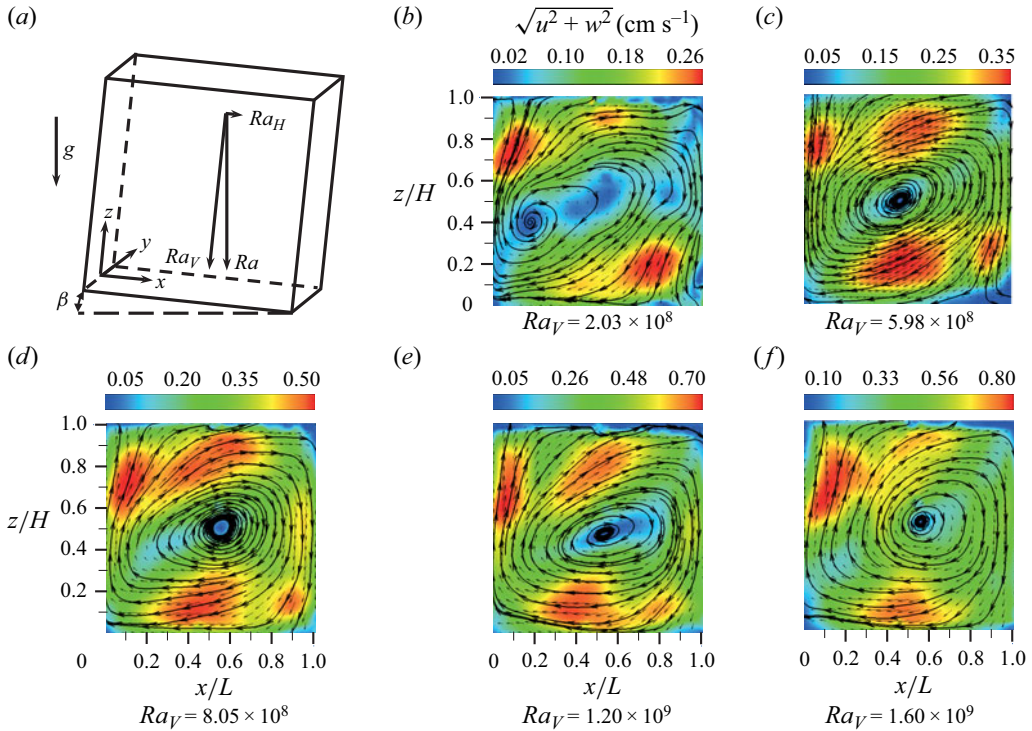


Figure 5. (a) Schematic diagram of the tilted convection cell, where Ra_V is the vertical Ra , Ra_H is the horizontal Ra , β is the tilt angle of the convection cell, and g is the acceleration of gravity. (b–f) Short-time averaged (over one turnover time) PIV velocity maps with streamlines for different Ra at $Pr = 244.2$ and $\beta = 1.5^\circ$.

the results obtained from direct numerical simulations by Shishkina & Horn (2016), who investigated a cylindrical RBC and found that at $\beta = 0$, multiple vortices were present in the flow field for $Ra = 10^6$ and $Pr = 100$. However, when $\beta > 0.9^\circ$, the multiple vortices are replaced by a single-roll LSC.

The change in the flow field is also reflected in the Fourier modes. Specifically, the flow field transitions from the dominance of the (2, 2) and (2, 1) modes at $\beta = 0$ (figure 2*i*) to the dominance of the (1, 1) mode at $\beta = 1.5^\circ$ (figure 6*a*). The energy contained in the other flow modes becomes relatively small, while the energy contained in the (1, 1) mode remains consistently above 0.6, and increases to above 0.8 with higher Ra_V ; when the cell is level, the energy contained in the (1, 1) mode is only from below 0.1 to approximately 0.2 in the same range of Ra . From the PIV velocity maps, we can calculate the horizontal and vertical Reynolds numbers as $Re_x = [\langle u^2 \rangle_{V,t}]^{1/2} H/\nu$ and $Re_z = [\langle w^2 \rangle_{V,t}]^{1/2} H/\nu$, respectively. Here, u and w represent horizontal and vertical velocities. Figure 6(b) presents the variations of Re_x and Re_z with Ra_V for $\beta = 0$ and $\beta = 1.5^\circ$ when $Pr = 244.2$. At $\beta = 0$, the flow field is always in the MRS, where the velocity in the horizontal direction is smaller than that in the vertical direction. As Ra increases, Re_x remains significantly smaller than Re_z . This is evident in the value of $\Lambda = Re_x/Re_z$, which is consistently below 0.6 for $\beta = 0$ (figure 6*c*). On the other hand, when $\beta = 1.5^\circ$ and the flow field transitions to the SRS, the velocity in the horizontal direction becomes comparable to that in the

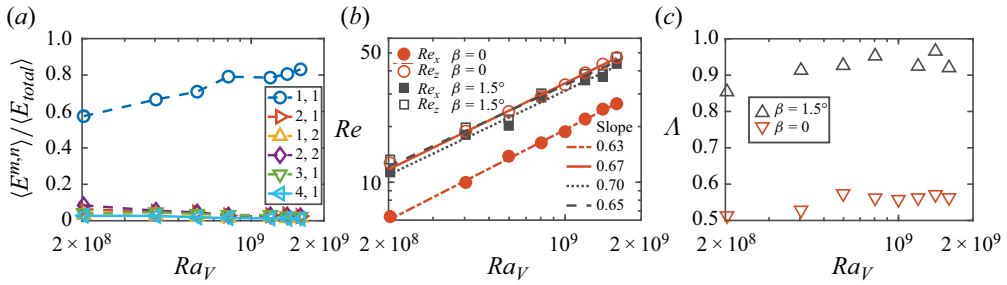


Figure 6. (a) Time-averaged energy contained in each flow mode as a function of Ra_V at $\beta = 1.5^\circ$. (b) The horizontal and vertical components of the Reynolds numbers Re_x and Re_z as functions of Ra_V for the cell level case ($\beta = 0$) and cell tilt case ($\beta = 1.5^\circ$). The dot-dashed line, solid line, dotted line and dashed line are the power-law fits to the data: $Re_x = 7.08 \times 10^{-5} Ra_V^{0.63}$ ($\beta = 0$), $Re_z = 3.35 \times 10^{-5} Ra_V^{0.67}$ ($\beta = 0$), $Re_x = 9.90 \times 10^{-6} Ra_V^{0.70}$ ($\beta = 1.5^\circ$) and $Re_z = 4.63 \times 10^{-5} Ra_V^{0.65}$ ($\beta = 1.5^\circ$), respectively. (c) The ratio of the horizontal and vertical components of the Reynolds number, $\Lambda = Re_x/Re_z$, as a function of Ra_V at $\beta = 0$ and $\beta = 1.5^\circ$. All the data are at $Pr = 244.2$.

vertical direction. As a result, as Ra_V increases, Re_x approaches Re_z . This is reflected by the fact that the value of Λ is near 0.9 at $\beta = 1.5^\circ$ (figure 6c), which is significantly larger than the values at $\beta = 0$. Moreover, from figure 6(b), we can see that Re_z at $\beta = 1.5^\circ$ is not significantly different from that at $\beta = 0$. This suggests that tilting the convection cell by 1.5° does not have a notable effect on the velocity in the vertical direction as we control the driving force in the vertical direction, i.e. Ra_V , to be the same for both $\beta = 0$ and $\beta = 1.5^\circ$. In contrast to Re_z , as shown in figure 6(b), Re_x at $\beta = 1.5^\circ$ exhibits a significant increase compared to $\beta = 0$. This indicates that the velocity in the horizontal direction experiences a substantial boost after tilting the convection cell. The increase in velocity is attributed to the influence of Ra_H . At $\beta = 0$, the flow in the horizontal direction in the RBC system is induced by vertical plumes (Xi *et al.* 2004). However, when $\beta = 1.5^\circ$, there is an additional source of horizontal flow introduced by Ra_H . In our experiment, the range of Ra_H is $5.28 \times 10^6 \leq Ra_H \leq 4.16 \times 10^7$. In horizontal convection, the critical Ra at which the flow becomes unsteady is below 1×10^6 when $Pr = 244.2$ (Hughes & Griffiths 2008), which is smaller than the Ra_H values applied in our experiment. Consequently, Ra_H provides the driving force for the horizontal flow in the convection cell. The horizontal driving force leads to a significant enhancement in the velocity in the horizontal direction compared to that observed at $\beta = 0$. In addition, from figure 6(b), we notice that when the cell is tilted, both Re_x and Re_z follow straight lines, and with almost identical slope, which is similar to the case when the cell is level. This validates the prediction by Grossmann & Lohse (2000) that if the LSC is created by tilting the cell at high Pr , the GL theory remains valid, as they predicted.

We have shown that at high Pr , a small angle tilt can induce greater horizontal flow and generate single-roll-like large-scale coherent flow. To examine whether this is the same at smaller Pr , we conducted experiments with a small tilted angle of the convection cell at low Pr values. At $Pr = 7.0$ and $\beta = 1.5^\circ$, figure 7(a) revealed a significant increase in the energy contained in the (1, 1) mode (from approximately 0.2–0.7 to approximately 0.6–0.8 in the same Ra range), indicating a stronger LSC, similar to that observed at $Pr = 244.2$. In contrast to the flow field at $Pr = 244.2$, when the cell is levelled, the flow fields at the current Ra range are all in the SRS, characterized by comparable vertical and horizontal velocities. This is evident in figure 7(c), where Λ remains larger than 0.7 over the entire

Pr dependence of flow topology in quasi-2-D RB convection

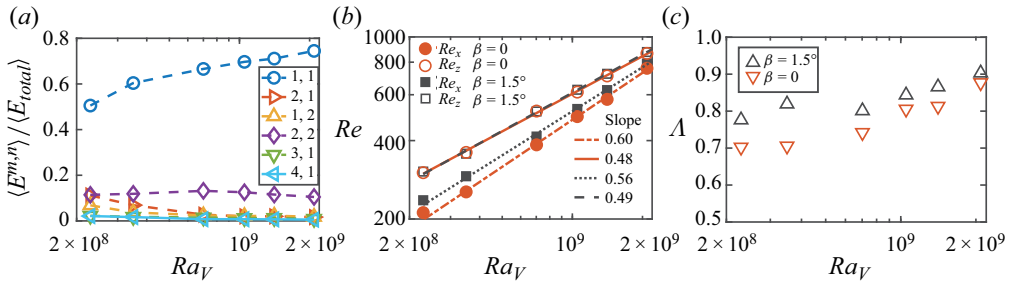


Figure 7. The same as in figure 6 but at $Pr = 7.0$. The dot-dashed line, solid line, dotted line and dashed line are the power-law fits to the data: $Re_x = 1.94 \times 10^{-3} Ra_V^{0.60}$ ($\beta = 0$), $Re_z = 2.94 \times 10^{-2} Ra_V^{0.48}$ ($\beta = 0$), $Re_x = 4.6 \times 10^{-3} Ra_V^{0.56}$ ($\beta = 1.5^\circ$) and $Re_z = 2.49 \times 10^{-2} v Ra_V^{0.49}$ ($\beta = 1.5^\circ$), respectively.

Ra range. Furthermore, figure 7(b) also showed that the vertical Reynolds number (Re_z) at $\beta = 1.5^\circ$ was not significantly different from that at $\beta = 0$, similar to that of $Pr = 244.2$. However, there was a slight increase in the horizontal Reynolds number (Re_x) at $\beta = 1.5^\circ$ compared to $\beta = 0$, which was also reflected in the increased value of Δ at $\beta = 1.5^\circ$ (figure 7c). This observation supports the idea that tilting the convection cell by a small angle increases the horizontal velocity, as reported in previous studies (Ahlers, Brown & Nikolaenko 2006; Guo *et al.* 2014; Shishkina & Horn 2016; Zwirner & Shishkina 2018; Jiang *et al.* 2019), and the increase of the horizontal velocity is stronger at higher Pr . This increase in horizontal velocity contributes to the formation and enhancement of the LSC. Overall, our findings suggest that horizontal velocity plays a crucial role in the formation of LSC. To establish the LSC, the horizontal velocity needs to be in accordance with the vertical velocity. And for high Pr flow, it is very hard to generate horizontal component flow due to the low thermal diffusion and high viscous damping. Thus an increase of horizontal velocity through a small angle tilt or other methods is crucial for the high Pr convection to have horizontal component and to form single-roll-formed LSC. These results provide insights into the mechanism and the control parameters of the occurrence of the different flow states, such as the MRS and SRS.

Another interpretation of the role of cell tilting in the formation of LSC suggests that the symmetry of the system is broken by the tilting of the cell, while there are two types of tilt: one is the tilt of the cell from the right, the other is the tilt of the cell from the left. When the cell is level, the buoyancy force is normal to the surface of the bottom plate, while when the cell is tilted from the right/left, the buoyancy force is no longer normal to the bottom plate: a component horizontal to the surface of the bottom plate (pointing to the right/left) emerges from the decomposition of the buoyancy force (as discussed in Zhang *et al.* 2021). This horizontal component of the buoyancy force induces horizontal component velocity in the right/left direction, thus facilitating the appearance of the LSC in the anticlockwise/clockwise direction. The one-to-one correspondence between the side of the tilt (right or left) and the direction of the LSC (anticlockwise or clockwise) implies that the causality is the following. The tilt of the cell breaks the symmetry, inducing horizontal buoyancy (the direction of the horizontal buoyancy depends on whether the cell is tilted from the right or the left side). Then this horizontal buoyancy induces horizontal velocity/motion, and after that, this horizontal velocity facilitates the appearance of the LSC. In this sense, the horizontal velocity is a consequence of the symmetry breaking, but the horizontal velocity is the cause of the appearance of the LSC. It is worth mentioning that

it was shown previously that the horizontal motion/velocity is crucial for the appearance of the LSC (Xi *et al.* 2004).

4. Discussion and conclusion

Our experimental results contribute to filling the gap in understanding the formation of the single-roll state (SRS) in Rayleigh–Bénard convection. First, Ra plays a crucial role: as the emergence of the SRS is typically observed at higher Ra , there is transitional Ra (Ra_t), only above which the flow transitions to SRS. And this transitional Ra scales with Pr as $Ra_t \sim Pr^{0.96}$ in the low Pr range, and $Ra_t \sim Pr^{3.3}$ in the high Pr range. The scaling in the low Pr range is consistent with the physical model of balance of time scale between energy dissipation and travel of plume that we proposed in our previous study (Chen *et al.* 2019), while the scaling in the high Pr range suggests the presence of a different governing mechanism.

We conjecture that the reason why increasing Pr hinders the formation of the large-scale circulation (LSC) is that with increasing Pr , the plumes are more likely to move vertically, thus it is harder to generate horizontal flow to facilitate the formation of the large-scale circulatory flow. In this regard, we tilt the convection cell by a small angle, deliberately inducing an additional horizontal driving force Ra_H . The presence of Ra_H leads to an increase in horizontal velocity, which promotes the formation of LSC.

Based on our findings, we can provide insights into previous experimental observations regarding the absence of LSC when Pr is high. First, it is important to acknowledge that the absence of LSC in the experiments conducted by Jiang *et al.* (2019) and Li *et al.* (2021) cannot be directly explained by our current study, as the parameter range of our experiments does not cover theirs. However, considering the similar geometry used in these studies, we propose attributing the absence of LSC to their chosen Ra values (5.0×10^8 and 5.0×10^9), which are far below the transitional Ra required for the LSC formation at the Pr values (480 and 651) in their studies; the data points obviously fall in the left region of the phase diagram. Nevertheless, it is important to note that Zhang *et al.* (1997) and Xi *et al.* (2004) observed the presence of LSC at even higher Pr values (895 and 596, respectively) and lower Ra values (5.0×10^8 and 5.0×10^9 , respectively) in aspect ratio one cubic/cylindrical cells. The discrepancy can be attributed to the different geometry of convection cells used in these studies, as demonstrated by Chong *et al.* (2018), who showed that larger aspect ratio Γ_y values facilitate the formation of the SRS. Specifically, Zhang *et al.* (1997) employed a cubic convection cell with a larger aspect ratio $\Gamma_y = 1.0$ compared to our experiments ($\Gamma_y = 0.3$). Similarly, the experiments conducted by Xi *et al.* (2004) used a cylindrical convection cell, which is similar to the cubic cell used in Zhang *et al.* (1997). Additionally, both studies tilted the convection cell to lock the direction of the LSC, a strategy validated in our current study as promoting the formation of the LSC.

In summary, our study reveals that the flow transitions from multiple-roll state (MRS) to SRS with increasing Ra , and the transition is hindered with increasing Pr . We mapped out a phase diagram on the flow topology change on Ra and Pr , and identified distinct flow topology transition with Ra for different Pr , and the scaling of the transitional Ra (Ra_t) on Pr . For the first time, the scaling of Re on Ra and Pr is acquired through full-field PIV velocity measurement. We also propose that increasing horizontal velocity benefits the formation of the LSC. To verify our conjecture, we introduce horizontal driving force Ra_H by tilting the convection cell with a small angle, which indeed leads to a transition from MRS to SRS at high Pr .

Pr dependence of flow topology in quasi-2-D RB convection

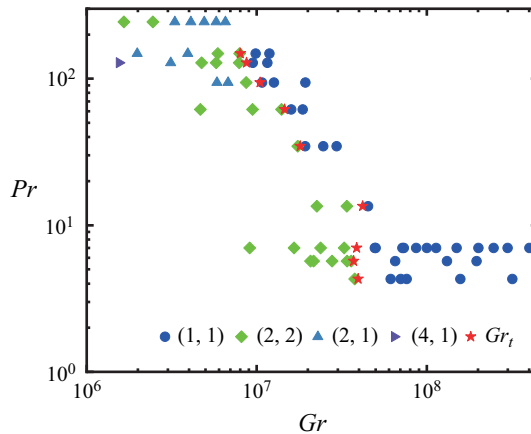




Figure 8. Phase diagram of the dominant Fourier modes in the Gr – Pr parameter space. The stars indicates the transitional Gr_t .

Funding. This work was supported by the National Natural Science Foundation of China (NSFC) under grant nos 12125204 and 12388101, the China Postdoctoral Science Foundation under grant no. 2021M702077, the Young Elite Scientists Sponsorship Program by CAST (2023QNRC001), and the 111 project of China (no. B17037).

Declaration of interests. The authors report no conflict of interest.

Author ORCIDs.

-  Xin Chen <https://orcid.org/0000-0001-9373-9696>;
-  Ao Xu <https://orcid.org/0000-0003-0648-2701>;
-  Heng-Dong Xi <https://orcid.org/0000-0002-2999-2694>.

Appendix

In figure 8, we present the phase diagram of dominant Fourier modes across a broad Gr – Pr parameter space. The phase diagram reveals that for low Pr values, the transitional Gr remains almost unchanged. However, for the high Pr regime, the transitional Gr decreases as Pr increases. This distinct behaviour with Pr at different regimes indicates the presence of different mechanisms governing the formation of the (1, 1) dominated flow state.

Table 2 summarizes the experimental parameters (Pr , Ra) and the measured results of Re for all the measurements in the present study.

While the PIV cannot directly provide information on individual or clusters of plumes, it does offer insights into the velocity field for different Pr and Ra . Given that the flow within the RBC is driven by plume motion, the velocity field data can yield quantitative insights relevant to our study. In figure 9, we present the ratio of the horizontal and vertical velocities as a function of Pr at nearly identical Ra of 1×10^9 . The figure illustrates that as Pr increases, the ratio decreases, indicating that the vertical component of the velocity becomes more and more dominant. This trend provides quantitative evidence supporting the observation that plumes tend to move predominantly in the vertical direction at higher Pr values.

<i>Pr</i>	<i>Ra</i>	<i>Re</i>	<i>Pr</i>	<i>Ra</i>	<i>Re</i>
7.0	2.29×10^8	409.0	128.5	2.00×10^8	17.7
	3.50×10^8	440.9		4.01×10^8	32.1
	5.13×10^8	533.7		6.08×10^8	41.0
	7.02×10^8	646.6		7.42×10^8	47.4
	1.05×10^9	788.5		1.01×10^9	59.1
	1.41×10^9	912.9		1.22×10^9	67.9
	1.73×10^9	993.3		1.48×10^9	79.3
13.5	3.05×10^8	239.3	148.3	2.94×10^8	21.4
	4.57×10^8	294.4		5.83×10^8	35.0
	6.10×10^8	345.0		8.76×10^8	46.2
34.6	6.03×10^8	151.9	244.2	1.17×10^9	58.3
	6.67×10^8	161.8		1.46×10^9	67.9
	8.51×10^8	180.7		1.76×10^9	79.5
	1.02×10^9	198.3		2.03×10^8	14.3
61.7	2.88×10^8	51.5	4.04×10^8	21.4	
	5.83×10^8	81.4	5.98×10^8	27.8	
	8.63×10^8	104.1	8.05×10^8	33.3	
	9.84×10^8	113.3	1.00×10^9	38.5	
	1.15×10^9	125.1	1.20×10^9	44.8	
94.3	5.50×10^8	53.5	1.41×10^9	50.1	
	6.40×10^8	58.9	1.60×10^9	54.2	
	8.19×10^8	68.7			
	1.01×10^9	80.1			
	1.19×10^9	88.5			
	1.82×10^9	116.4			

Table 2. Experimental parameters (*Pr*, *Ra*) and the measured results of *Re* for all the measurements in the present study.

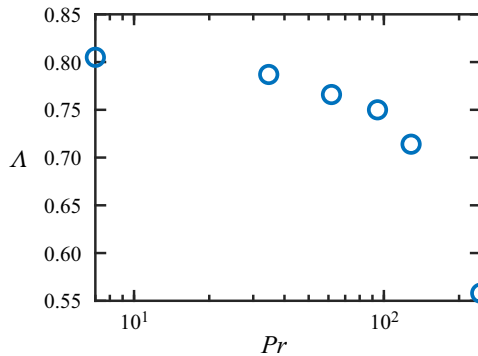


Figure 9. The ratio of the horizontal and vertical velocities as a function of *Pr* at nearly identical *Ra* of 1×10^9 .

REFERENCES

- AHLERS, G., BROWN, E. & NIKOLAENKO, A. 2006 The search for slow transients, and the effect of imperfect vertical alignment, in turbulent Rayleigh–Bénard convection. *J. Fluid Mech.* **557**, 347–367.
- AHLERS, G., GROSSMANN, S. & LOHSE, D. 2009 Heat transfer and large scale dynamics in turbulent Rayleigh–Bénard convection. *Rev. Mod. Phys.* **81** (2), 503–537.
- BROWN, E. & AHLERS, G. 2006 Rotations and cessations of the large-scale circulation in turbulent Rayleigh–Bénard convection. *J. Fluid Mech.* **568**, 351–386.
- BROWN, E. & AHLERS, G. 2009 The origin of oscillations of the large-scale circulation of turbulent Rayleigh–Bénard convection. *J. Fluid Mech.* **638**, 383–400.
- CHANDRA, M. & VERMA, M.K. 2011 Dynamics and symmetries of flow reversals in turbulent convection. *Phys. Rev. E* **83** (6), 067303.
- CHANDRA, M. & VERMA, M.K. 2013 Flow reversals in turbulent convection via vortex reconnections. *Phys. Rev. Lett.* **110** (11), 114503.
- CHEN, X., HUANG, S.-D., XIA, K.-Q. & XI, H.-D. 2019 Emergence of substructures inside the large-scale circulation induces transition in flow reversals in turbulent thermal convection. *J. Fluid Mech.* **877**, R1.
- CHEN, X., WANG, D.-P. & XI, H.-D. 2020 Reduced flow reversals in turbulent convection in the absence of corner vortices. *J. Fluid Mech.* **891**, R5.
- CHEN, X., XU, A., XIA, K.-Q. & XI, H.-D. 2023 The effect of the cell tilting on the temperature oscillation in turbulent Rayleigh–Bénard convection. *Phys. Fluids* **35** (8), 085141.
- CHILLA, F. & SCHUMACHER, J. 2012 New perspectives in turbulent Rayleigh–Bénard convection. *Eur. Phys. J. E* **35** (7), 58.
- CHONG, K.-L., WAGNER, S., KACZOROWSKI, M., SHISHKINA, O. & XIA, K.-Q. 2018 Effect of Prandtl number on heat transport enhancement in Rayleigh–Bénard convection under geometrical confinement. *Phys. Rev. Fluids* **3** (1), 013501.
- CIONI, S., CILIBERTO, S. & SOMMERIA, J. 1996 Experimental study of high-Rayleigh-number convection in mercury and water. *Dyn. Atmos. Oceans* **24** (1–4), 117–127.
- CIONI, S., CILIBERTO, S. & SOMMERIA, J. 1997 Strongly turbulent Rayleigh–Bénard convection in mercury: comparison with results at moderate Prandtl number. *J. Fluid Mech.* **335**, 111–140.
- GROSSMANN, S. & LOHSE, D. 2000 Scaling in thermal convection: a unifying theory. *J. Fluid Mech.* **407**, 27–56.
- GUO, S.-X., ZHOU, S.-Q., CEN, X.-R., QU, L., LU, Y.-Z., SUN, L. & SHANG, X.-D. 2014 The effect of cell tilting on turbulent thermal convection in a rectangular cell. *J. Fluid Mech.* **762**, 273–287.
- HUANG, S.-D., KACZOROWSKI, M., NI, R. & XIA, K.-Q. 2013 Confinement-induced heat-transport enhancement in turbulent thermal convection. *Phys. Rev. Lett.* **111** (10), 104501.
- HUGHES, G.O. & GRIFFITHS, R.W. 2008 Horizontal convection. *Annu. Rev. Fluid Mech.* **40**, 185–208.
- JIANG, L., SUN, C. & CALZAVARINI, E. 2019 Robustness of heat transfer in confined inclined convection at high Prandtl number. *Phys. Rev. E* **99** (1), 013108.
- KRISHNAMURTI, R. & HOWARD, L.N. 1981 Large-scale flow generation in turbulent convection. *Proc. Natl Acad. Sci. USA* **78** (4), 1981–1985.
- LAM, S., SHANG, X.-D., ZHOU, S.-Q. & XIA, K.-Q. 2002 Prandtl number dependence of the viscous boundary layer and the Reynolds numbers in Rayleigh–Bénard convection. *Phys. Rev. E* **65** (6), 066306.
- LI, X.-M., HE, J.-D., TIAN, Y., HAO, P. & HUANG, S.-D. 2021 Effects of Prandtl number in quasi-two-dimensional Rayleigh–Bénard convection. *J. Fluid Mech.* **915**, A60.
- LI, Y.-Z., CHEN, X., XU, A. & XI, H.-D. 2022 Counter-flow orbiting of the vortex centre in turbulent thermal convection. *J. Fluid Mech.* **935**, A19.
- LOHSE, D. & XIA, K.-Q. 2010 Small-scale properties of turbulent Rayleigh–Bénard convection. *Annu. Rev. Fluid Mech.* **42** (1), 335–364.
- VAN DER POEL, E.P., STEVENS, R.J.A.M., SUGIYAMA, K. & LOHSE, D. 2012 Flow states in two-dimensional Rayleigh–Bénard convection as a function of aspect-ratio and Rayleigh number. *Phys. Fluids* **24** (8), 085104.
- QIU, X.-L. & TONG, P. 2001 Large-scale velocity structures in turbulent thermal convection. *Phys. Rev. E* **64** (3), 036304.
- REN, L., TAO, X., ZHANG, L., NI, M.-J., XIA, K.-Q. & XIE, Y.-C. 2022 Flow states and heat transport in liquid metal convection. *J. Fluid Mech.* **951**, R1.
- SHISHKINA, O. & HORN, S. 2016 Thermal convection in inclined cylindrical containers. *J. Fluid Mech.* **790**, R3.
- SUGIYAMA, K., NI, R., STEVENS, R.J., CHAN, T.-S., ZHOU, S.-Q., XI, H.-D., SUN, C., GROSSMANN, S., XIA, K.-Q. & LOHSE, D. 2010 Flow reversals in thermally driven turbulence. *Phys. Rev. Lett.* **105** (3), 034503.

- TROPEA, C., YARIN, A.L. & FOSS, J.F. 2007 *Springer Handbook of Experimental Fluid Mechanics*, vol. 1. Springer.
- VOGT, T., HORN, S., GRANNAN, A.M. & AURNOU, J.M. 2018 Jump rope vortex in liquid metal convection. *Proc. Natl Acad. Sci. USA* **115** (50), 12674–12679.
- WAGNER, S. & SHISHKINA, O. 2013 Aspect-ratio dependency of Rayleigh–Bénard convection in box-shaped containers. *Phys. Fluids* **25** (8), 085110.
- WANG, Q., VERZICCO, R., LOHSE, D. & SHISHKINA, O. 2020 Multiple states in turbulent large-aspect-ratio thermal convection: what determines the number of convection rolls? *Phys. Rev. Lett.* **125** (7), 074501.
- WEI, P. 2021 The persistence of large-scale circulation in Rayleigh–Bénard convection. *J. Fluid Mech.* **924**, A28.
- WEISS, S. & AHLERS, G. 2011 Turbulent Rayleigh–Bénard convection in a cylindrical container with aspect ratio $\Gamma = 0.50$ and Prandtl number $Pr = 4.38$. *J. Fluid Mech.* **676**, 5–40.
- XI, H.-D., LAM, S. & XIA, K.-Q. 2004 From laminar plumes to organized flows: the onset of large-scale circulation in turbulent thermal convection. *J. Fluid Mech.* **503**, 47–56.
- XI, H.-D. & XIA, K.-Q. 2007 Cessations and reversals of the large-scale circulation in turbulent thermal convection. *Phys. Rev. E* **75**, 066307.
- XI, H.-D. & XIA, K.-Q. 2008 Flow mode transitions in turbulent thermal convection. *Phys. Fluids* **20** (5), 055104.
- XI, H.-D., ZHANG, Y.-B., HAO, J.-T. & XIA, K.-Q. 2016 Higher-order flow modes in turbulent Rayleigh–Bénard convection. *J. Fluid Mech.* **805**, 31–51.
- XI, H.-D., ZHOU, Q. & XIA, K.-Q. 2006 Azimuthal motion of the mean wind in turbulent thermal convection. *Phys. Rev. E* **73**, 056312.
- XI, H.-D., ZHOU, S.-Q., ZHOU, Q., CHAN, T.-S. & XIA, K.-Q. 2009 Origin of the temperature oscillation in turbulent thermal convection. *Phys. Rev. Lett.* **102** (4), 044503.
- XIA, K.-Q. 2013 Current trends and future directions in turbulent thermal convection. *Theor. Appl. Mech. Lett.* **3** (5), 052001.
- XIA, K.-Q., LAM, S. & ZHOU, S.-Q. 2002 Heat-flux measurement in high-Prandtl-number turbulent Rayleigh–Bénard convection. *Phys. Rev. Lett.* **88** (6), 064501.
- XIA, K.-Q., SUN, C. & ZHOU, S.-Q. 2003 Particle image velocimetry measurement of the velocity field in turbulent thermal convection. *Phys. Rev. E* **68**, 066303.
- ZHANG, J., CHILDRESS, S. & LIBCHABER, A. 1997 Non-Boussinesq effect: thermal convection with broken symmetry. *Phys. Fluids* **9** (4), 1034–1042.
- ZHANG, L., DING, G.-Y. & XIA, K.-Q. 2021 On the effective horizontal buoyancy in turbulent thermal convection generated by cell tilting. *J. Fluid Mech.* **914**, A15.
- ZHU, X.-J., MATHAI, V., STEVENS, R.J.A.M., VERZICCO, R. & LOHSE, D. 2018 Transition to the ultimate regime in two-dimensional Rayleigh–Bénard convection. *Phys. Rev. Lett.* **120** (14), 144502.
- ZWIRNER, L. & SHISHKINA, O. 2018 Confined inclined thermal convection in low-Prandtl-number fluids. *J. Fluid Mech.* **850**, 984–1008.